Explainable Radiomics based on Association of Histopathological Cell Density and Multiparametric MR Radiomic Features for High-Risk Stratification of Prostate Cancer Patients

Yusuke Shibayama MS[1,2], shibayama.yusuke.756@m.kyushu-u.ac

Hidetaka Arimura PhD[3*], arimura.hidetaka.616@m.kyushu-u.ac.jp

Yukihisa Takayama MD, PhD[4*], ytakayama@fukuoka-u.ac.jp

Fumio Kinoshita MD, PhD[5], fumio@med.kyushu-u.ac.jp

Dai Takamatsu, MD[5], daiatama1021@gmail.com

Akihiro Nishie MD, PhD[6], akihironishie@gmail.com

Satoshi Kobayashi MD, PhD[5], kobayashi.satoshi.282@m.kyushu-u.ac.jp

Takashi Matsumoto MD, PhD[5], matsumoto.takashi.971@m.kyushu-u.ac.jp

Masaki Shiota MD, PhD[5], shiota.masaki.101@m.kyushu-u.ac.jp

Masatoshi Eto MD, PhD[5], eto.masatoshi.717@m.kyushu-u.ac.jp

Yoshinao Oda MD, PhD[7], oda.yoshinao.389@m.kyushu-u.ac.jp

Kousei Ishigami MD, PhD[8], ishigami.kosei.581@m.kyushu-u.ac.jp

[1] Department of Medical Technology, Kyushu University Hospital, Fukuoka, Japan,

[2] Department of Health Sciences, Graduate School of Medical Sciences, Kyushu University, Fukuoka, Japan

[3] Department of Health Sciences, Faculty of Medical Sciences, Kyushu University, Fukuoka, Japan

[4] Departments of Radiology, Faculty of Medicine, Fukuoka University, Fukuoka, Japan

[5] Department of Urology, Graduate School of Medical Sciences, Kyushu University, Fukuoka, Japan

[6] Department of Radiology, Graduate School of Medical Science, University of the Ryukyus, Okinawa, Japan

[7] Department of Anatomic Pathology, Pathological Sciences, Graduate School of Medical Sciences, Kyushu University, Fukuoka, Japan

[8] Department of Clinical Radiology, Graduate School of Medical Sciences, Kyushu University, Fukuoka, Japan

* Corresponding authors:

Hidetaka Arimura, PhD, arimura.hidetaka.616@m.kyushu-u.ac.jp

Department of Health Sciences, Faculty of Medical Sciences, Kyushu University, 3-1-1 Maidashi, Higashi-ku, Fukuoka 812-8582, Japan; +81-92-641-1151

Yukihisa Takayama MD, PhD, ytakayama@fukuoka-u.ac.jp

Departments of Radiology, Faculty of Medicine, Fukuoka University, 7-45-1 Nanakuma, Jonan-ku, Fukuoka 814-0180, Japan; +81-92-871-6631-

Authors' Contribution: Yusuke Shibayama: Study conception and design/Acquisition of data/Analysis and interpretation of data/Drafting of manuscript/Critical revision. Hidetaka Arimura: Study conception and design/Acquisition of data/Analysis and interpretation of data/Drafting of manuscript/Critical revision. Yukihisa Takayama: Acquisition of data/Analysis and interpretation of data/ Critical revision. Fumio Kinoshita: Acquisition of data/Analysis and interpretation of data/ Critical revision. Dai Takamatsu: Acquisition of data/Analysis and interpretation of data/ Critical revision. Akihiro Nishie: Acquisition of data/Analysis and interpretation of data/ Critical revision. Satoshi Kobayashi: Acquisition of data/Analysis and interpretation of data/ Critical revision. Takashi Matsumoto: Acquisition of data/Analysis and interpretation of data/ Critical revision. Masaki Shiota:

Acquisition of data/Analysis and interpretation of data/ Critical revision. Masatoshi Eto: Acquisition of data/Analysis and interpretation of data/ Critical revision. Yoshinao Oda: Acquisition of data/Analysis and interpretation of data/ Critical revision. Kousei Ishigami: Acquisition of data/Analysis and interpretation of data/ Critical revision.

Declaration of Interest: The authors have no conflict of interests

Ethical approval: This retrospective study was approved by the institutional review board of Kyushu University Hospital, Japan (Approval number: [2020-472]).

Data Availability Statement: The datasets generated and/or analyzed during the current study are available from the corresponding author on reasonable request.

Acknowledgments

This study was partially supported by grant from Japan Society for the Promotion of Science KAKENHI Grant numbers JP24K10840. The authors would like to express our sincere thanks to all

members of the Arimura laboratory (https://web.shs.kyushu-u.ac.jp/~arimura/index.html) and all members of the Kyushu university hospital for their valuable comments for this study.

Abstract

Objective: This study aimed to develop an explainable radiomics model for stratifying prostate cancer (PCa) patients with high-risk disease via investigation of the association between cell density (CD) in the PCa region on histopathological images and multiparametric MR (mpMR) radiomics features.

Materials and Methods: A total of 137,970 radiomic features were calculated from mpMR images (101 PCa regions of 44 patients), and joint histograms (JHs) were derived from dynamic contrast-enhanced (DCE) images for each PCa region. The association between CD on histopathological images and its corresponding mpMR radiomic features in PCa regions for various grade groups and the three risk groups was evaluated using Spearman's correlation coefficient. To validate the potential of the radiomic-feature-CD association, we developed the radiomics model for stratifying patients into low/intermediate-risk and high-risk groups.

Results: There were moderate correlations of the CD with a DCE-based texture feature (WV_HH_1st_GLSZM_ZP) (ρ=0.609, p=0.024) and DCE-JH feature (JH_WV_HL_1st versus 5th-1st_Hist_STD) (ρ=0.609, p=0.024) in the high-risk group. The radiomics model had an accuracy of 0.920 for stratifying the patients of a test dataset into the low/intermediate-risk and high-risk groups.

Conclusion: The association between CD and mpMR features can be leveraged to develop the

explainable radiomics for the high-risk stratification of patients with PCa.

Keywords: mpMRI, radiomics, cell density, prostate cancer

1. Introduction

Histopathological images have been widely used to evaluate the Gleason score (GS) and determine treatment strategies in prostate cancer (PCa). The GS reflects tumor aggressiveness and is based on cell density, size, and shape [1-3]. The 2014 International Society of Urological Pathology (ISUP) comprehensively defines grade groups (GGs) from the GS system [1]. For localized PCa, the initial treatment options can be decided according to the risk group, which is determined mainly based on the clinical T-stage, GG, and prostate-specific antigen (PSA) level [4]. In particular, patients with high-risk prostate cancer are recommended to undergo radical prostatectomy or external radiation therapy, which has shown similar effectiveness, but different adverse events [5]. Moreover, high-risk patients are most often treated using conformal dose escalated radiation therapy with androgen deprivation [6]. Since there was no statistically significant difference in the incidence of prostate cancer specific mortality between the low- and intermediate- risk groups [7], we focused on the stratification of prostate cancer patients into two groups, high-risk and low/intermediate risk groups in this study.

Multiparametric prostate magnetic resonance imaging (mpMRI) is also crucial in the detection, localization, characterization, risk stratification, surveillance, and determination of treatment strategies for PCa [8-11]. The mpMRI assesses focal lesions and anatomical information using multiple imaging parameters including diffusion-weighted imaging (DWI), T1-weighted

105 imaging (T1WI), T2-weighted imaging (T2WI), and dynamic contrast-enhanced (DCE) imaging.
106 Many studies have reported correlations between the GS or cell density on histopathological images
107 and the apparent diffusion coefficient (ADC) obtained from DW images with multiple *b*-values [12-
108 14]. This association is mainly because the increased cellularity of malignant lesions causes lower
109 ADCs owing to the restriction of motion of water in the reduced extracellular spaces. Although the
110 relationship between DW images and cell density has been discussed in other literatures [15-17],
111 studies on the correlation between other mpMRI features and cell density are insufficient. Therefore,
112 we focused on cell density and explored its correlation with mpMRI radiomic features.

113 The Prostate Imaging Reporting and Data System (PI-RADS) has been used to improve the
114 early diagnosis and treatment of prostate cancer [18]. Despite its usefulness, the PI-RADS appears to
115 have limitations, including relatively poor specificity and inconsistent interpretations among readers
116 [19]. Consequently, we assumed that quantitative approaches and mpMR radiomics models could
117 support PI-RADS in definitively diagnosing PCa [19]. The mpMR radiomics models can quantify
118 subtle imaging feature patterns that are difficult for human vision [8,9,20,21]. To leverage radiomics
119 models as tools in clinical settings, they should be explainable in terms of the outputs of the models
120 [22]. The Royal Society defines *explainable* as “implying that a wider range of users can understand
121 why or how a conclusion was reached” [22]. We define *explainable radiomics* as “radiomics that a
122 wider range of medical users can understand why the image features in a radiomics were deployed

for a specific disease, how they were calculated, and how the radiomics outputted conclusions". The associations of mpMR image features with histopathological findings and cell density could explain why image features can be utilized for classifying PCa patients into low/intermediate-risk and high-risk groups.

However, to our best knowledge, no study has investigated the explainable radiomics models for the risk group stratification of patients with PCa based on the association between cell density and mpMR radiomic features for various GGs and the three risk groups. Two applications of the radiomics models are as follows: GG or risk group change can be monitored by calculating mpMR features in the MR-linac [23], and the clinical target volume (CTV) can be modified according to the risk group change during treatment [24].

Thus, this study aimed to investigate the association of cell density on histopathological images of radical prostatectomy specimens with radiomics features on mpMRI in PCa regions and to develop an explainable radiomics model for stratifying PCa patients into the low/intermediate-risk and high-risk groups.

2. Materials and methods

2.1 Study design and patients

This retrospective study was approved by the institutional review board of Kyushu University Hospital, Japan (Approval number: [2020-472]).

Forty-four patients (median age: 65 years; range: 55–74 years; Stage: T1–T3a, N0, M0; median PSA: 7.80 ng/ml; range: 4.28–33.65 ng/ml) with PCa who received preoperative magnetic resonance imaging (MRI) and underwent radical prostatectomy between August 2010 and August 2014 were evaluated. The radical prostatectomies were performed by two urologists with over 6 years of experience (M.S. and M.E.). Radical prostatectomy specimens were processed as previously described [25]. All cancer regions were outlined as references on hematoxylin and eosin-stained histopathological images digitized with a whole slide scanner (Nanozoomer-SQ; Hamamatsu Photonics KK) at 20× magnification with a pixel size of 0.4 μm based on the mutual consensus between two pathologists with over 6 years of experience (F.K. and D.T.). All GS and GG for all prostate cancer regions were determined by two urologists with over 6 years of experience (T.M. and S.K.).

Table 1 lists the sequence parameters of PCa MRI protocols. All 44 patients with PCa were scanned using a 3.0 T scanner (Achieva, Philips Healthcare) with four sequences of spin-echo T1WI, T2WI, DWI, and DCE imaging. ADC maps were derived from DW images at *b*-values of 0, 1000, and 2000 s/mm^2. DCE images with gradient-recalled echo T1WI were acquired at ten phases from the pre-contrast phase (1st to 8th phases with an interval of 10 s) to the delayed phase (240 s), using

158 gadolinium diethylenetriamine pentaacetic acid (Gd-DTPA, Bayer HealthCare) as a contrast agent.
159 Consequently, the 16 types of images, including spin-echo T1W image, T2W image, three DW images
160 at b-values of 0, 1000, and 2000 s/mm², ADC map, and ten DCE images at ten phases were acquired
161 for each patient.

162 We generated 2D JHs between different phases of DCE or subtraction phases of DCE (SPD)
163 images to visualize temporally changing perfusion patterns in the tumor foci, as described previously
164 [21]. A JH is a 2D image to visualize the association between the intensities of corresponding pixels
165 in two images [26]. Isotropic images with an isovoxel size of 0.391 mm (mode pixel size in four
166 sequences) were produced using a linear interpolation algorithm from anisotropic MR images with
167 in-plane pixel sizes different from the slice thicknesses. All MR images, including the JHs, were
168 converted into 8-bit images prior to all computational processes.

169 Contours of 101 PCa regions (1 to 5 regions per patient) were delineated on a single slice
170 with the maximum diameter for each PCa region on isotropic ADC maps fused with DW images at
171 a *b*-value of 1000 corresponding to the PCa region in the histopathological images. This was
172 performed using 3D slicer version 4.10.1 [27]. The cancer regions on the prostate specimens
173 corresponding to the cancer regions were delineated on the ADC maps based on a mutual consensus
174 between two radiologists with over 6 years of experience (Y.T. and A.N.). Each contour of the PCa
175 region was placed on a slice of the 16 types of images with the same 3D coordinates (*x*, *y*, and *z*) as

the world coordinates of the MR scanner. The two radiologists ensured that the prostate displacements caused by anatomical changes were tolerable in the 16 types of MR images.

In total, 101 PCa regions from 44 patients were separated into a training dataset (n=34 patients, 76 regions, 75%) to construct of the radiomics models and a test dataset (n=10, 25 regions, 25%) for evaluation of the models.

Table 1 Sequence parameters in MRI protocols for prostate cancer

	T1WI	**T2WI**	**DWI**	**DCE imaging**
Repetition time (ms)	401	4000	4000	6.65
Echo time (ms)	10.4	90	68	3.26
Flip angle (deg.)	90	90	90	20
Field of view (mm)	200	200	300	250
Matrix size (mm)	512×512	512×512	288×288	256×256
Pixel size (mm)	0.391	0.391	1.04	0.977
Slice thickness (mm)	4.00	4.00	4.00	2.00
Slice gap (mm)	5.50	5.50	5.50	1.00
b-value (s/mm^2)	n/a	n/a	0, 1000, 2000	n/a
No. of images	20	20	20	80

Abbreviations: T1WI, T1-weighted imaging; T2WI, T2-weighted imaging; DWI, diffusion weighted imaging; DCE, dynamic contrast-enhanced.

2.2 Cell density on histopathological image

Figure 1 shows the procedure for measuring the cell density in a cancerous region. The contour on an ADC map represents the cancerous region delineated by radiologists according to a dark area with the low ADCs. On the other hand, the contour on a slice of the radical prostatectomy specimen was determined by pathologists. There are mainly two reasons why the contours in those images are different. One is the different observers and viewpoints, and the other is the time differences between the MR scanning and radical prostatectomy, which were longer than two months in our dataset. The number of cells (C) and the area of the cancerous region (S) on histopathological images obtained from the specimen were measured using the open-source software QuPath (version 0.2.0) (https://qupath.github.io/) [28]. Cell density was calculated as the number of cells in a tumor region divided by the area of the cancer region: $\mathrm{C\ (cells)\ /\ S\ (mm^2)}$.

A criterion for the valid registration between the ROIs on ADC map and histopathological images was determined based on 10 cancer regions (2 regions for each grade group of 10 different patients) using the Dice similarity coefficient (DSC). DSC is the degree of agreement between the two ROIs and is considered as the registration accuracy of the two ROIs between the mpMR and histopathological images. The average DSC was 0.79 ± 0.12, indicating a moderate level of the registration accuracy. From this result, a criterion of DSC > 0.5 was determined for the valid registration.

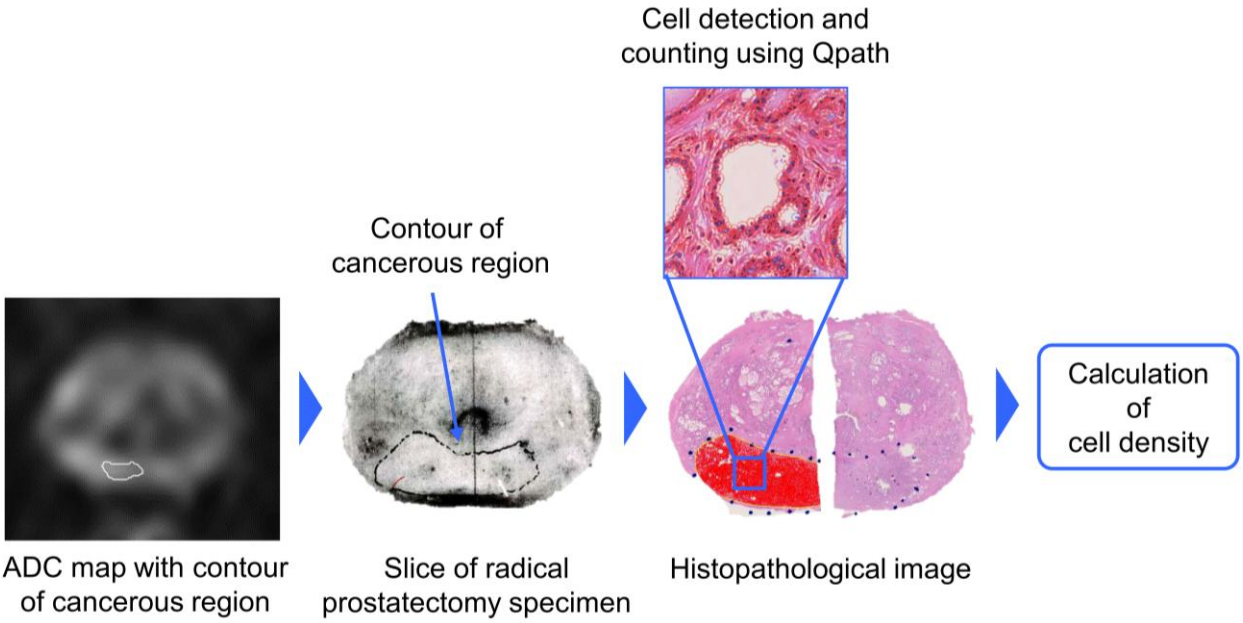

204

205 **Fig. 1** Procedure for measuring the cell density in a cancerous region. The contour on the ADC map
206 represents the cancerous region delineated by radiologists. The prostate specimen with a black
207 contour depicts the corresponding lesion area on the prostatectomy specimen, as delineated by
208 pathologists, and the cell density of the lesion was measured on the pathological image obtained from
209 the prostate specimen.

210

211 **2.3 Radiomic features on mpMRI**

212 In a previous study [21], 137,970 features were extracted from 16 types of MR images and
213 495 joint histograms (JHs). The JH is a 2D image used to visualize the association between the
214 intensities of corresponding pixels in two images [26]. Six significant mpMRI features, including

three DCE subtraction JH features [JH_6th versus Delayed-5th_GLSZM_LGZE, JH_WV_LL_1st versus 2nd-1st_Hist_STD, JH_WV_HL_1st versus 5th-1st_Hist_STD], two DCE image features [WV_HH_3rd_Hist_Max, WV_HH_1st_GLSZM_ZP], and one ADC map feature [WV_HH_ADC_GLRLM_LGRE] (Table 2) were selected from 137,970 features to mitigate overfitting problem using the least absolute shrinkage and selection operator (LASSO) algorithm [21]. This is because the number of image features should be less than 10% of the number of patients in the training dataset (n=34 patients in this study) [29,30]. Therefore, the number of features should be less than or equal to 3 (34 / 10 = 3.4) in this study. The features were selected from histogram and texture features of DWI, T1WI, T2WI, DCE images, and JHs and four wavelet-filtered images to stratify the PCa patients into low (GG ≤2) and high (GG ≥3) GGs [21]. The histogram and texture features were then obtained using a MATLAB-based radiomics tools package (MathWorks, MATLAB ver. R2023a) [20].

Four wavelet-filtered images were generated using four combinations of low-(L) and high-pass (H) 2D wavelet filters (Coiflet); these were LL, LH, HL, and HH. The texture features were a gray-level co-occurrence matrix (GLCM), a gray-level run-length matrix (GLRLM), a gray-level size-zone matrix (GLSZM), and a neighborhood gray-tone difference matrix (NGTDM). The histogram feature was referred to as Hist. These radiomic features were employed under the assumption that they reflected histological properties (i.e., cell density) in the cancer region.

Table 2 Significant features of mpMR images and joint histogram images for stratifying the PCa patients into the low (≤2) and high (≥3) GGs

mpMRI image	Significant features
DCE subtraction JH image	JH_6th versus Delayed-5th_GLSZM_LGZE
	JH_WV_LL_1st versus 2nd-1st_Hist_STD
	JH_WV_HL_1st versus 5th-1st_Hist_STD
DCE	WV_HH_3rd_Hist_Max
	WV_HH_1st_GLSZM_ZP
ADC	WV_HH_ADC_GLRLM_LGRE

Abbreviations: DCE, dynamic contrast-enhanced; JH, joint histogram; ADC, apparent diffusion coefficient; A-B, subtraction between A and B; H, high-pass filter Hist, histogram; JH_A versus B, joint histogram between A and B; L, low-pass filter; WV, wavelet; GLSZM, gray level size zone matrix; LGZE, low gray level zone emphasis; ZP, zone percentage; GLRLM, gray level run-Length matrix; LGRE, low gray level run emphasis; STD, standard deviation.

2.4 Construction of a risk group stratification model

To validate the potential associations between radiomic features and cell density, we developed a radiomics model using a support vector machine (SVM) for stratifying patients into the low/intermediate-risk and high-risk groups. SVM can finesse the curse of dimensionality, which means that as the number of features that you use increases, the amount of data that you need to increase exponentially to build generalized models [31,32]. Figure S1 shows the workflow for

training, testing, and evaluating the SVM model for PCa. The SVM models were built using Gaussian, linear, and polynomial kernels with soft-margin parameters. Patients in the high-risk group were divided into training and test datasets to ensure an approximately equal distribution of cancer regions within each dataset. The cancerous regions of each patient belong to the same dataset (training or testing).

The hyperparameters corresponding to the three kernels of the SVM models were optimized using a Bayesian optimization method [33] with leave-one-out cross-validation (LOOCV) to maximize the area under the curve (AUC) of the receiver operating characteristic curve of the training dataset. The model was evaluated based on its AUC, accuracy, sensitivity, and specificity for the training and test datasets. The SVM was performed using MathWorks MATLAB ver. R2023a.

2.5 Statistical analysis

The normality of cell density distributions in each group was assessed using histograms and the Kolmogorov–Smirnov test. Continuous and categorical variables were compared using Student's *t*-test. Correlations between cell density and mpMR radiomic features were analyzed for each group. All cell densities and features were normalized using a Z-score ([value–mean)/(standard deviation]) for each group. Correlations between normalized cell density and each radiomic feature were analyzed using the Spearman's rank correlation test. The correlations were then evaluated as

weak ($0.00 \leq |\rho| \leq 0.39$), moderate ($0.40 \leq |\rho| \leq 0.69$), or strong ($0.70 \leq |\rho| \leq 1.00$) [34]. All statistical analyses were performed using MathWorks MATLAB ver. R2023a. The significance threshold was set at $p < 0.05$.

3. Results

3.1 Patients

Table 3 shows the patient characteristics. All cancer regions were stratified into a low GG (GG ≤2) (GS 3+3 and 3+4 [n=67]) and a high GG (GG ≥3) (GS 4+3 and above [n=34]) following the ISUP Guideline 2014 [1] after radical prostatectomy. In addition, the cancer regions were classified as being low (GS ≤6 [n=28]), intermediate (GS=7 [n=59]), and high (GS ≥8 [n=14]) risk corresponding to the National Comprehensive Cancer Network guideline [4]. The cancer regions comprised 34 lesions in the transition zone (TZ) and 67 in the peripheral zone (PZ).

281 **Table 3** Clinical characteristics of the patients and cancer regions

Variables		**Value**	
Total number of patients		44	
Total number of cancer regions		101	
Cancer location (region)			
TZ		34	
PZ		67	
Age (years) [min–max (median)]		55–74 (65)	
Prostate-specific antigen (ng/ml) [PSA, min–max (median)]		4.28–33.65 (7.80)	
Number of cancer regions (TZ, PZ)			
GG 1 (GS ≤ 6)		28 (10,18)	
GG 2 (GS 3 + 4 = 7)		39 (13,26)	
GG 3 (GS 4 + 3 = 7)		20 (8,12)	
GG 4 (GS 8)		6 (3,3)	
GG 5 (GS 9,10)		8 (3,5)	
According to ISUP GGs		**Corresponding to NCCN classification**	
GG ≤ 2	67 (23,44)	**Low**	28 (10,18)
GG ≥3	34 (14,20)	**Intermediate**	59 (21,38)
		High	14 (6,8)

282 Abbreviations: TZ, Transition zone; PZ, peripheral zone; GG, grade group; GS, Gleason score; ISUP,
283 International Society of Urological Pathology; NCCN, National Comprehensive Cancer Network.
284

3.2 Cell density on histopathological image

The average cell densities for the low and high GGs were 5160 cells/mm^2 and 5670 cells/mm^2, respectively, with a significant difference (p=0.025). Figure 2 (a) shows the violin plots of the cell densities for the low and high GGs. Figure 2 (b) shows the violin plots of cell densities for the low-, intermediate-, and high-risk cancer regions. The average cell densities for the low-, intermediate-, and high-risk groups were 5229, 5282, and 6104 cells/mm^2, respectively. Significant differences were observed between the low- and high-risk groups (p=0.021) and between the intermediate- and high-risk groups (p=0.020). Figure 2 (d) shows the violin plots of cell density for GGs 1, 2, 3, and GG 4 + GG 5 cancer regions. The average cell densities for GGs 1, 2, 3, and GG 4 + GG 5 were 5229, 5276, 5295, and 6104 cells/mm^2, respectively. There were significant differences between GG 1 and GG 4 + GG 5 (p=0.021), GG 2 and GG 4 + GG 5 (p=0.034), and GG 3 and GG 4 + GG 5 (p=0.047). Although the average cell density of the low-risk group was lower than that of the intermediate-risk group, there was no significant difference between the two groups. Figure 2 (c) shows the violin plots of cell density for TZ and PZ lesions. There were no significant differences between the TZ and PZ lesions (TZ: 5272 and PZ: 5445 cells/mm^2, p=0.443).

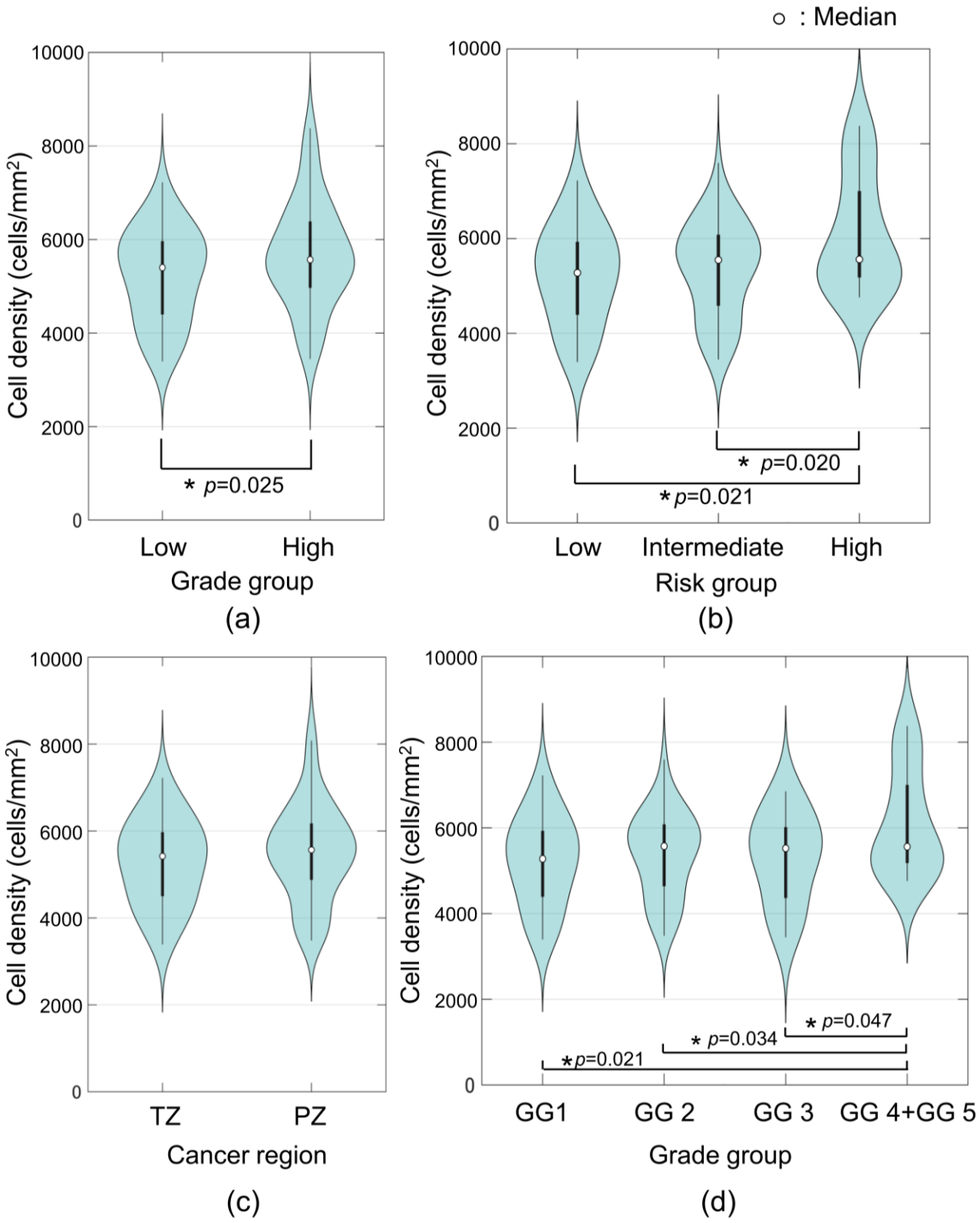

Fig. 2 Violin plots illustrating the distribution of cell density, with the median (open circle) and

interquartile range (thick line) shown for each risk group (a) Low (GG ≤2, GS 3+3 and 3+4) and high (GG ≥3, GS 4+3 and above) GGs. (b) Low-, intermediate-, and high-risk groups. (c) TZ and PZ lesions. (d) GG 1, GG 2, GG 3, and GG 4 + GG 5.

3.3 Correlations between cell density and radiomic features

Figure 3 shows a heatmap of Spearman's rank correlation coefficient ρ and indicates the statistical significance differences (significance threshold: *: $p<0.05$) between the cell density and all features in each risk group. The cell density was significantly correlated with WV_HH_ADC_GLRLM_LGRE for the low GG group (ρ=-0.326, p=0.013) and with JH_WV_LL_1st versus 2nd-1st_Hist_STD for the high GG group (ρ=-0.363, p=0.016). The Spearman's rank correlation coefficient showed that in the high-risk group, WV_HH_1st_GLSZM_ZP (ρ=0.609, p=0.024) and JH_WV_HL_1st versus 5th-1st_Hist_STD (ρ=0.609, p=0.024) had the strongest correlation with the cell density in cancer regions. A moderate correlation with WV_HH_1st_GLSZM_ZP (ρ=0.538, 0.050) was also observed. No radiomic feature showed significant correlation in the low-risk and intermediate-risk groups ($|\rho| \leq 0.275$, $0.148 \leq p$).

Figure 4 shows the three PCa regions on the histopathological images (upper row), their corresponding 1st DCE images (middle row), and the 5th DCE images (bottom row). The left column

shows a GG 1 PCa region (4875 cells/mm^2, GS 3+3) for a low-risk group patient. The center and right columns show a GG 4 region (5219 cells/mm^2, GS 4+4) and GG 5 region (7751 cells/mm^2, GS 5+4) for the two high-risk group patients, respectively. White contours represent PCa regions in the DCE images.

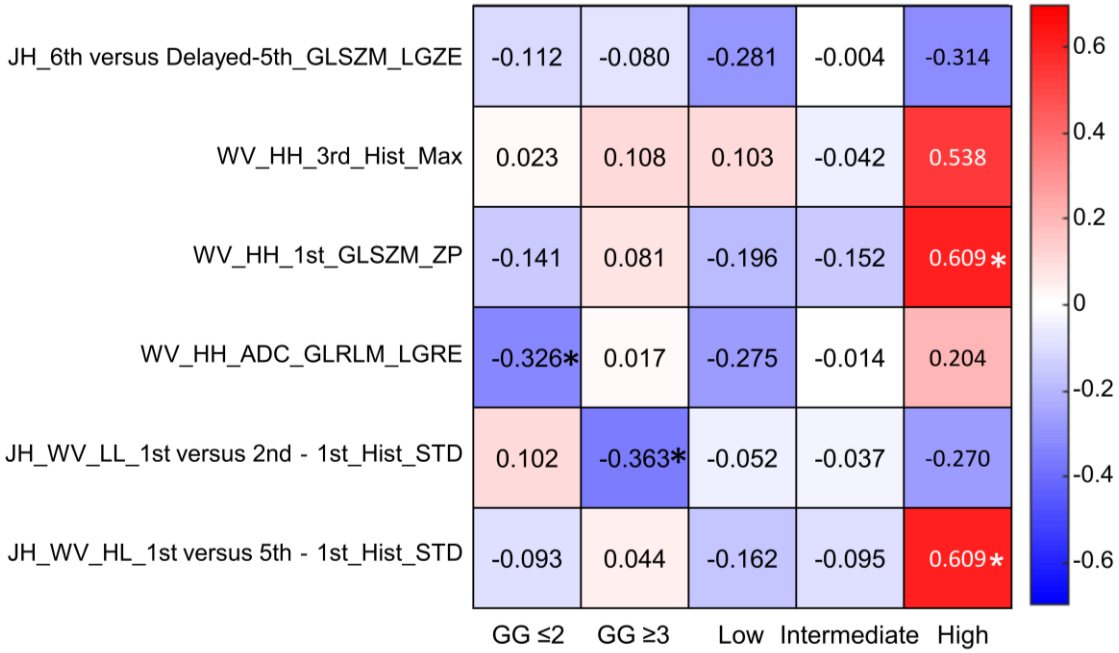

Fig. 3 Heatmap of Spearman's rank correlation coefficient ρ between the cell density and all features in each risk group (significance threshold: *: p<0.05). GG, grade group; ADC, apparent diffusion coefficient; A-B, subtraction between A and B; H, high-pass filter Hist, histogram; JH, joint histogram; JH_A versus B, joint histogram between A and B; L, low-pass filter; WV, wavelet; GLSZM, gray level size zone matrix; LGZE, low gray level zone emphasis; ZP, zone percentage; GLRLM, gray level run-Length matrix; LGRE, low gray level run emphasis; STD, standard deviation

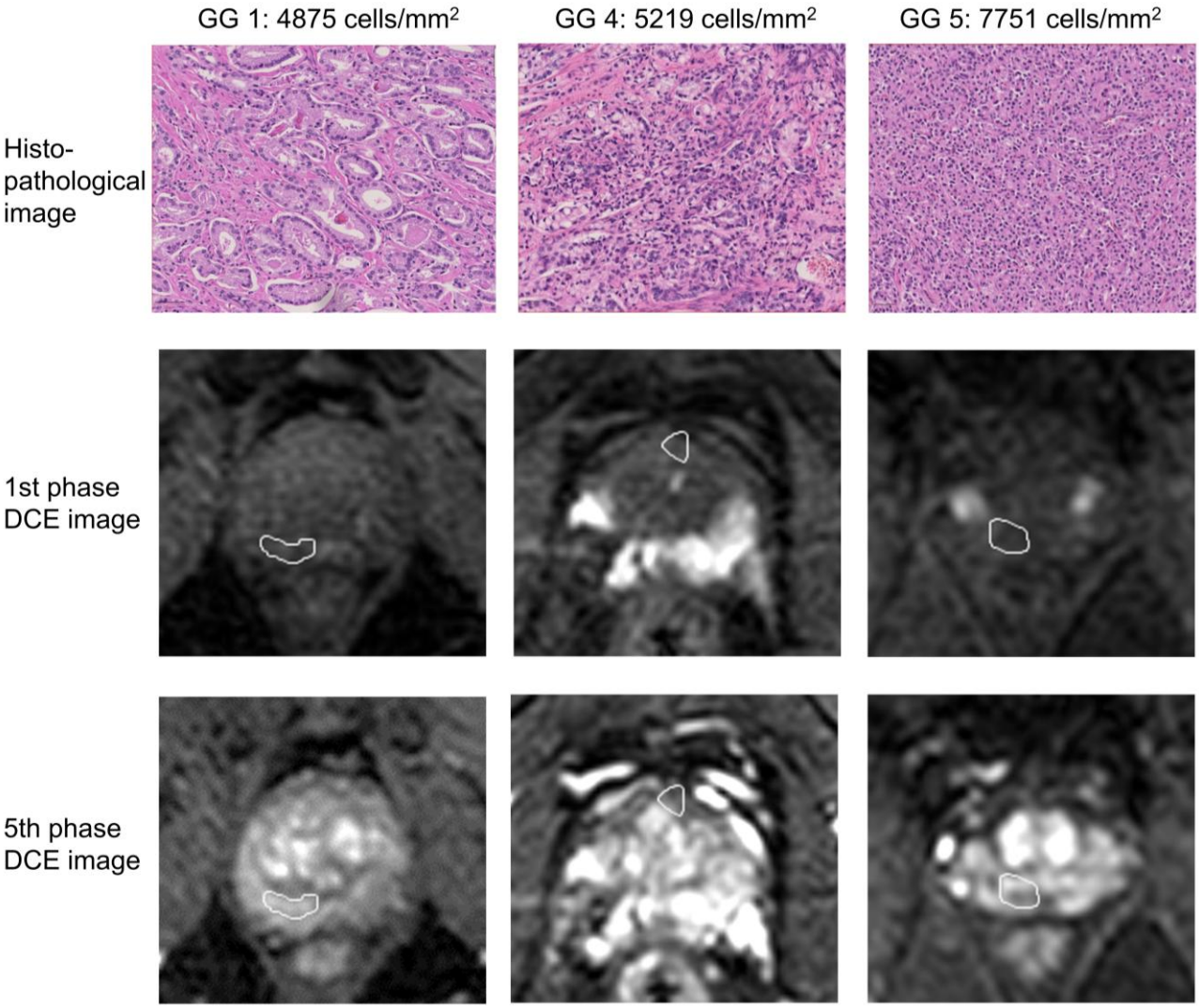

331

332 **Fig. 4** Three PCa regions on the histopathological images (upper row), their corresponding 1st DCE

333 images (middle row), and 5th DCE images (bottom row). White contours represent PCa regions in

334 the DCE images.

335

336 **3.4 Model performance for risk stratification**

The average computation time of the radiomics model for each patient was 22.6 second in total (feature calculation time: 22.2 second, stratification time: 0.4 second). The two mpMRI features ([WV_HH_1st_GLSZM_ZP] and [JH_WV_HL_1st versus 5th-1st_Hist_STD]) associated with cell density were used to build the model. The optimal kernel of the SVM was a cubic polynomial function. The optimal threshold of the SVM outputs of 0.3 was found so that patients could be best stratified into low-/intermediate-risk and high-risk groups. The AUC, accuracy, sensitivity, and specificity for risk stratification for the training dataset were 0.920, 0.895, 0.364, and 0.940, respectively. The AUC, accuracy, sensitivity, and specificity for the risk stratification for the test dataset were 0.758, 0.920, 0.333, and 0.957, respectively.

4. Discussion

In our study, *explainable radiomics* was defined as "radiomics that a wider range of medical users can understand why the image features in a radiomics were deployed for a specific disease, how they were calculated, and how the radiomics outputted conclusions". The mpMR features of a DCE-based texture feature (WV_HH_1st_GLSZM_ZP) and DCE-JH feature (JH_WV_HL_1st versus 5th-1st_Hist_STD) were deployed for our radiomics model because they were associated with cell density in the high-risk group patients found in this study. The method used to calculate the features was explained in our previous study [21] and this study, and the output (conclusion) of the radiomics was

355 calculated from the SVM, which is well understood. Therefore, the proposed model could be
356 considered as an explainable radiomics approach.

357 Figure 4 shows the three PCa regions on the histopathological images and its corresponding
358 1st DCE image and 5th DCE images. There were no prostate cells in the luminal space of normal
359 prostate glands. In contrast, the components of predominantly poorly formed/fused/cribriform glands
360 increased as the GS or GG increased. GG 5 (GS 9-10) lacked gland formation, and the prostate cancer
361 cells were arranged in sheets. This is consistent with what *Epstein et al.* [1] have reported.
362 Consequently, cell density increased as the GS or GG increased.

363 A negative correlation of ADC values with cell density in PCa has been previously described
364 [12,35]. Each tumor cell exerts a force on another cell remotely from a distance, without physical
365 contact [36]. The contact force attracts tumor cells to each other during physical contact. These two
366 forces result in increased cell density within highly malignant tumors, restricting diffusion within the
367 tumor and leading to low ADC values. Thus, the ADC indicates PCa aggressiveness [37-40]. A
368 previous study has reported the use of ADC in detecting PCa and evaluating its aggressiveness [41].

369 In addition to $ADC_{mean,}$ the ADC_{10th} percentile has also been proposed as a biomarker of PCa
370 aggressiveness because it reflects the highest GG tumor found in a given lesion [39]. Therefore, we
371 considered that the radiomic features in DWI or ADC images may be strongly correlated with cell
372 density. However, the results indicated that cell density was correlated only with

373 WV_HH_ADC_GLRLM_LGRE in patients with low GG (Fig. 3). Although ADC could differentiate
374 GG 2 (GS 3+4) from GG 3 (4+3) PCa, consistent with previous studies [42-44], ADC might not be
375 suitable for subdividing malignancy within each group. This could explain why ADC radiomics
376 features were not correlated with cell density in the high-risk group.

377 Cell density had significant correlations with one DCE radiomic feature of
378 WV_HH_1st_GLSZM_ZP in the high-risk group and two JH radiomic features of JH_WV_LL_1st
379 versus 2nd-1st_Hist_STD in the high GG and with JH_WV_HL_1st versus 5th-1st_Hist_STD in the
380 high-risk group (Fig. 3). Both JH radiomic features are the standard deviations of the pixel values on
381 the wavelet-filtered JH between the 1st phase DCE images and 2nd-1st phase or 5th-1st phase SPD
382 images. This result indicates that in the high-risk group, PCa regions with higher cell density had
383 variations in pixel values on the JHs from the mean value. The WV_HH_1st_GLSZM_ZP and
384 JH_WV_LL_1st versus 2nd-1st_Hist_STD features correspond to early enhancement. The
385 JH_WV_HL_1st versus 5th-1st_Hist_STD characterizes the combination of early enhancement and
386 washout.

387 Unlike normal tissues, cancer tissues often demonstrate early enhancement and washout
388 owing to the high cell density in their voxels, high microvessel density (MVD), and high GS [5,12,45].
389 Several studies have shown that the MVD as an independent predictor of the pathological stage in
390 PCa may be related to tumor aggressiveness [46,47]. In addition, MVD is associated with DCE-MRI

391 pharmacokinetic parameters such as volumetric transfer constant (K^{trans}), plasma volume fraction (v_p),
392 and extravascular extracellular space (v_e) [12,48,49]. The enhancement effect on DCE images was
393 previously reported to show a significant difference only between high-risk tumors (GS ≥4+4) [12,45].
394 This finding suggests that neovascularization in prostate cancer may develop rapidly in high-risk
395 tumors, which is consistent with our study showing that DCE images are associated with pathological
396 malignancy in the high-risk group.

397 Although several studies have demonstrated improvements in risk classification accuracy
398 using mpMRI-based radiomics, research on the relationship between these radiomic features and
399 pathological findings have been limited [17,21,44]. Our study addresses this gap by showing that
400 DCE features, which are effective for the risk stratification, are associated with cellular density in
401 high-risk groups, thereby serving as explainable radiomics. This effectively associates radiomic
402 features with pathological findings in PCa. These results indicate that DCE radiomic features reflect
403 pathological conditions in high-risk groups, thereby enhancing our understanding of both the
404 pathological and imaging characteristics.

405 Despite the limited role of DCE-MRI in PI-RADS v2, it is a required protocol for mpMR
406 examinations to detect PCa [5,41]. However, in contrast, several studies reported that combining DCE
407 images with DWI images improves diagnostic performance [45,50]. Furthermore, The DCE radiomic
408 features appear to reflect the properties of cell density in high-risk PCa and may allow for more

409 detailed grading.

410 Consequently, the radiomics model used to stratify patients with PCa into low/intermediate-
411 risk and high-risk groups achieved accuracies of 0.895 and 0.920 for training and test datasets,
412 respectively, based on significant features associated with cell density. Since the accuracy for the test
413 dataset was higher than that for the training dataset, the impact of overfitting was considered minimal.
414 Predicting cancer aggressiveness using the radiomics model may be possible by identifying the areas
415 of high cell counts; thus, the change in the risk group in PCa could be monitored during radiation
416 therapy with an MR linac [23]. Moreover, because the definition of the PCa CTV in radiation therapy
417 depends on the risk classification [24], the CTV can be adaptively modified according to the risk
418 group change during treatment.

419 The proposed model demonstrates a high specificity of 0.957, meaning that there are fewer
420 cases where high-risk tumors are mistakenly identified as positives (false positives). The model can
421 accurately identify only truly high-risk tumors, reducing the risk of unnecessary exposure and surgical
422 treatments, minimizing the risk of side effects and contributing to functional preservation. However,
423 the low sensitivity of 0.333 indicates that some high-risk tumors may have been missed (false
424 negatives), which could lead to insufficient dose escalation and, therefore, suboptimal treatment for
425 some patients. This highlights the need for improving sensitivity in future models to ensure that all
426 clinically significant tumors are targeted effectively.

The two features ([WV_HH_1st_GLSZM_ZP] and [JH_WV_HL_1st versus 5th-1st_Hist_STD]) had the moderate correlation with PCa cell density in high-risk groups. According to the rule of thumb, the number of features should be less than 10% of the number of patients in the training dataset to mitigate these problems [29,30]. Since the number of features should be less than or equal to three (34 training patients / 10 = 3.4) for this study, the number of two features was appropriate. Nevertheless, the use of a small number of features may cause bias and overfitting or underfitting problems, thereby reducing the model robustness [50,51]. To overcome these problems, the number of patients should be increased for selecting more features in future works. Therefore, we could investigate the relationships between mpMR image features and additional pathological biomarkers (other than cell density) such as MVD [45,52,53], architecture, size, shape of tumor cells [54], cancer volume fractions, and epithelial/lumen cell ratios [55,56], which were not used in the current study. Integrating mpMR features correlated with the pathological biomarkers could potentially improve the explainability and performance of the high-risk stratification model in future works.

Our study had some limitations. First, the sample size was limited to 44 patients, which affected the generalization of the proposed model. Even though we reduced the number of features to two to avoid overfitting, we must increase the number of patients by monitoring the generalization metrics [57] in future works. Second, the present study did not divide patients according to PCa

location into TZ and PZ lesions because the number of patients was limited. There was no statistically significant difference in cell density between the TZ and PZ lesions (TZ: 5272 and PZ: 5445 cells/mm^2, p=0.443) in our study. Barral et al. [47] also reported no significant difference in glandular density between the TZ and PZ in high-grade high GG groups. However, Barral et al. [47] compared the ADC_{mean} and glandular density of GS 3+3 TZ-PCa with those of PZ-PCa, and reported that the ADC_{mean} of TZ-PCa with GS 3+3 was significantly lower than that of PZ-PCa with GS 3+3. Thus, selecting features from TZ and PZ could boost the performance of the proposed radiomics model developed in future works.

Third, radiomic features other than the six mpMR radiomic features selected by *Urakami et al.* [21] were not considered in the investigation of the association with cell density. Thus, possible features with higher LASSO coefficients should be analyzed. Moreover, radiomic features from additional mpMRI protocols, such as amide proton transfer (APT) imaging or chemical exchange saturation transfer (CEST) imaging, were not explored because these protocols were not employed for PCa patients in our hospital. Several studies have reported that the optimization of mpMRI techniques, including PCa, can improve the accuracy of cancer detection or grading including that of PCa [58,59]. CEST imaging enables radiologists to detect in vivo metabolites through the continual exchange of labile protons with water [40]. *Takayama et al.* [58] reported correlation between the GS and APT signal intensities. Thus, radiomic features for CEST imaging might have a significant

correlation with cell density and could reflect histopathological features more appropriately.

Finally, correlations were investigated only for cell density in PCa regions as a histopathological variable. As mentioned above, we can explore the associations between mpMR image features and other pathological biomarkers, such as MVD [45,52,53], architecture, size, shape of tumor cells [54], cancer volume fractions, and epithelial/lumen cell ratios [55,56]. Particularly, previous studies have reported an association between MVD and GS, and DCE-MRI features could potentially aid in stratifying GS [42,52,53]. The associations with these pathological biomarkers could enhance the explainability and performance of the high-risk stratification model in future works.

5. Conclusions

We found that cell density was associated with DCE radiomics features in the high-risk PCa group. The associations between radiomics features and cell density were leveraged for developing an explainable radiomics model for stratification of PCa patients into the low/intermediate-risk and high-risk groups. This study suggests that utilizing the explainable radiomics model may be beneficial for monitoring treatment efficacy and explaining the reason of radiomics output to PCa patients.

References

1. Epstein JI, Egevad L, Amin MB et al (2016) The 2014 international society of urological pathology (ISUP) consensus conference on Gleason grading of prostatic carcinoma definition of grading patterns and proposal for a new grading system. Am J Surg Pathol 40(2):244-252.

2. Epstein JI (2018) Prostate cancer grading: a decade after the 2005 modified system. Mod Pathol 31(S1):S47-63.

3. Mohler JL, Antonarakis ES, Armstrong AJ et al (2019) Prostate Cancer, Version 2.2019, NCCN Clinical Practice Guidelines in Oncology. J Natl Compr Canc Netw 17(5):479-505.

4. Schaeffer EM, Srinivas S, Adra N et al (2023) Prostate Cancer, Version 4.2023, NCCN Clinical Practice Guidelines in Oncology. J Natl Compr Canc Netw 21(10):1067-1096.

5. Brawley S, Mohan R, Nein CD (2018). Localized prostate cancer: treatment options. American family physician 97(12):798-805.

6. Saad A, Goldstein J, Lawrence YR et al (2017) Classifying high-risk versus very high-risk prostate cancer: is it relevant to outcomes of conformal radiotherapy and androgen deprivation? Radiation Oncol 12:1-8.

7. King MT, Nguyen PL, Boldbaatar N et al (2018) Long-term outcomes of partial prostate treatment with magnetic resonance imaging-guided brachytherapy for patients with favorable-

497 risk prostate cancer. Cancer 124(17):3528–3535.

498 8. Weinreb JC, Barentsz JO, Choyke PL et al (2016) PI-RADS prostate imaging – reporting and
499 data system: 2015, Version 2. Eur Urol 69(1):16-40.

500 9. Turkbey B, Rosenkrantz AB, Haider MA et al (2019) Prostate imaging reporting and data system
501 version 2.1: 2019 update of prostate imaging reporting and data system version 2. Eur Urol 76(3):
502 340-351.

503 10. Kızılay F, Çelik S, Sözen S et al (2020) Correlation of prostate-imaging reporting and data
504 scoring system scoring on multiparametric prostate magnetic resonance imaging with
505 histopathological factors in radical prostatectomy material in Turkish prostate cancer patients: a
506 multicenter study of the Urooncology Association. Prostate Int 8(1):10-15.

507 11. Zhu LY, Ding XF, Huang TB et al (2020) Correlation analysis between prostate imaging report
508 and data system score and pathological results of prostate cancer. Natl Med J China 00(34): 2663-
509 2668.

510 12. Hötker AM, Mazaheri Y, Aras Ö et al (2015) Assessment of Prostate Cancer Aggressiveness by
511 Use of the Combination of Quantitative DWI and Dynamic Contrast-Enhanced MRI. AJR Am J
512 Roentgenol 206(4):756-63.

13. Glazer DI, Hassanzadeh E, Fedorov A et al (2017) Diffusion-weighted endorectal MR imaging at 3T for prostate cancer: correlation with tumor cell density and percentage Gleason pattern on whole mount pathology. Abdom Radiol 42(3):918-925.

14. Manetta R, Palumbo P, Gianneramo C et al (2019) Correlation between ADC values and Gleason score in evaluation of prostate cancer: multicentre experience and review of the literature. Gland Surg Suppl S216-S222.

15. Verma S, Rajesh A, Morales H et al (2011) Assessment of aggressiveness of prostate cancer: correlation of apparent diffusion coefficient with histologic grade after radical prostatectomy. Am J Roentgenol 196(2):374-381.

16. Boesen L, Chabanova E, Løgager V et al (2015) Apparent diffusion coefficient ratio correlates significantly with prostate cancer gleason score at final pathology. J Magn Reson Imaging 42(2):446-453.

17. Vos EK, Kobus T, Litjens GJ et al (2015) Multiparametric Magnetic Resonance Imaging for Discriminating Low-Grade From High-Grade Prostate Cancer. Invest Radiol 50(8):490-497.

18. American College of Radiology (n.d.) PI-RADS: Prostate Imaging-Reporting and Data System. ACR.org. https://www.acr.org/Clinical-Resources/Reporting-and-Data-Systems/PI-RADS. Accessed 18 December 2024

19. Li M, Yang L, Yue Y et al (2021) Use of Radiomics to Improve Diagnostic Performance of PI-RADS v2.1 in Prostate Cancer. Front Oncol 17;10:631831.

20. Vallières M, Freeman CR, Skamene SR et al (2015) A radiomics model from joint FDG-PET and MRI texture features for the prediction of lung metastases in soft-tissue sarcomas of the extremities. Phys Med Biol 60(14):5471-5496.

21. Urakami A, Arimura H, Takayama Y et al (2022) Stratification of prostate cancer patients into low- and high-grade groups using multiparametric magnetic resonance radiomics with dynamic contrast-enhanced image joint histograms. Prostate 82:330-344.

22. The Royal Society (2019) Explainable AI: The Basics. Policy Briefing Available online at: https://royalsociety.org/-/media/policy/projects/explainable-ai/ai-and-interpretability-policy-briefing.pdf. Accessed 18 December 2024

23. Winkel D, Bol GH, Kroon PS et al (2019) Adaptive radiotherapy: The Elekta Unity MR-linac concept. Clin Transl Radiat Oncol 18:54-59.

24. Boehmer D, Maingon P, Poortmans P et al (2006) EORTC radiation oncology group. Guidelines for primary radiotherapy of patients with prostate cancer. Radiother Oncol 79(3):259-69.

25. Hossain A, Arimura H, Kinoshita F et al (2020) Automated approach for estimation of grade groups for prostate cancer based on histological image feature analysis. Prostate 80(3):291-302.

547 26. Hill D, Hawkes DJ (2009) Handbook of Medical Image Processing and Analysis. 2nd ed. MA:
548 Academic Press.

549 27. Fedorov A, Beichel R, Kalpathy-Cramer J et al (2012) 3D Slicer as an Image Computing
550 Platform for the Quantitative Imaging Network. Magnetic Resonance Imaging 30(9):1323-41.

551 28. Bankhead P, Loughrey MB, Fernández JA et al (2017) QuPath: open source software for digital
552 pathology image analysis. Sci Rep 7(1):1–7.

553 29. Peduzzi P, Concato J, Kemper E et al (1996) A simulation study of the number of events per
554 variable in logistic regression analysis. J Clin Epidemiol 49(12):1373-9.

555 30. Jain AK, Duin RPW, Mao J (2000) Statistical pattern recognition: a review. IEEE Trans Pattern
556 Anal Mach Intell 22(1):4–37.

557 31. Hastie T, Tibshirani R, Friedman J (2009) The Elements of Statistical Learning: Data Mining,
558 Inference, and Prediction. Second Edition. Springer, New York, p.443

559 32. Bishop CM, Nasrabadi NM (2006) Pattern recognition and machine learning Vol.4, Springer,
560 New York

561 33. Gelbart MA, Jasper S, and Ryan PA (2014) Bayesian optimization with unknown constraints.
562 arXiv preprint arXiv:1403.5607.

563 34. Schober P, Boer C, Schwarte LA (2018) Correlation Coefficients: Appropriate Use and
564 Interpretation. Anesth Analg 126(5):1763-1768.

565 35. Gibbs P, Liney GP, Pickles MD et al (2009) Correlation of ADC and T2 measurements with cell
566 density in prostate cancer at 3.0 Tesla. Invest Radiol 44(9):572-576.

567 36. Nakano T, Okaie Y, Kinugasa Y et al (2020) Roles of Remote and Contact Forces in Epithelial
568 Cell Structure Formation. Biophys J 118(6):1466-1478.

569 37. Vargas HA, Akin O, Franiel T et al (2011) Diffusion-weighted endorectal MR imaging at 3 T for
570 prostate cancer: tumor detection and assessment of aggressiveness. Radiology 259(3):775-784.

571 38. Donati OF, Mazaheri Y, Afaq A et al (2014) Prostate cancer aggressiveness: assessment with
572 whole-lesion histogram analysis of the apparent diffusion coefficient. Radiology 271(1):143-152.

573 39. Bollineni VR, Kramer G, Liu Y et al (2015) A literature review of the association between
574 diffusion-weighted MRI derived apparent diffusion coefficient and tumour aggressiveness in
575 pelvic cancer. Cancer Treat Rev 41(6):496-502.

576 40. Oto A, Kayhan A, Jiang Y et al (2010) Prostate cancer: differentiation of central gland cancer
577 from benign prostatic hyperplasia by using diffusion-weighted and dynamic contrast-enhanced
578 MR imaging. Radiology 257(3):715-723.

579 41. Tamada T, Prabhu V, Li J et al (2017) Assessment of prostate cancer aggressiveness using

apparent diffusion coefficient values: impact of patient race and age. Abdom Radiol 42(6):1744-1751.

42. Feng Z, Min X, Margolis DJA et al (2017) Evaluation of different mathematical models and different b-value ranges of diffusion-weighted imaging in peripheral zone prostate cancer detection using b-value up to 4500 s/mm2. PLoS One 12:e0172127.

43. Alessandrino F, Taghipour M, Hassanzadeh E et al (2019) Predictive role of PI-RADSv2 and ADC parameters in differentiating Gleason pattern 3 + 4 and 4 + 3 prostate cancer. Abdom Radiol 44:279-285.

44. Borren A, Groenendaal G, Moman MR et al (2014) Accurate prostate tumour detection with multiparametric magnetic resonance imaging: dependence on histological properties. Acta Oncol 53(1):88-95.

45. Brawer MK (1996) Quantitative microvessel density. A staging and prognostic marker for human prostatic carcinoma. Cancer 78:345–932.

46. Schlemmer HP, Merkle J, Grobholz R et al (2004) Can pre-operative contrastenhanced dynamic MR imaging for prostate cancer predict microvessel density in prostatectomy specimens? Eur Radiol 14:309–317.

47. Barral M, Jemal-Turki A, Beuvon F et al (2020) Cellular density of low-grade transition zone

prostate cancer: A limiting factor to correlate restricted diffusion with tumor aggressiveness. Eur J Radiol 131:109230.

48. Bagher-Ebadian H, Brown SL, Ghassemi MM et al (2023) Dynamic contrast enhanced (DCE) MRI estimation of vascular parameters using knowledge-based adaptive models. Scientific Reports 13(1), 9672.

49. Abreu-Gomez J, Lim C, Cron GO et al (2021) Pharmacokinetic modeling of dynamic contrast-enhanced (DCE)-MRI in PI-RADS category 3 peripheral zone lesions: preliminary study evaluating DCE-MRI as an imaging biomarker for detection of clinically significant prostate cancers. Abdom Radiol 46(9):4370-4380.

50. Hua J, Xiong Z, Lowey J, Suh E, Dougherty ER (2005) Optimal number of features as a function of sample size for various classification rules. Bioinformatics 15:21(8):1509-15.

51. Aliferis C, Simon G (2004) Artificial Intelligence (AI) and Machine Learning (ML) for Healthcare and Health Sciences: The Need for Best Practices Enabling Trust in AI and ML. Springer, New York

52. Erbersdobler A, Isbarn H, Dix K et al (2010) Prognostic value of microvessel density in prostate cancer: a tissue microarray study. World J Urol 28(6):687-92.

53. Singanamalli A, Rusu M, Sparks RE et al (2015) Identifying in vivo DCE MRI markers associated with microvessel architecture and gleason grades of prostate cancer. J Magn Reson Imaging 43(1):149-58.

54. Sant GR, Knopf KB, Albala DM (2017) Live-single-cell phenotypic cancer biomarkers-future role in precision oncology? NPJ Precis Oncol 15:1(1):21.

55. Chatterjee A, Bourne RM, Wang S et al (2018) Diagnosis of Prostate Cancer with Noninvasive Estimation of Prostate Tissue Composition by Using Hybrid Multidimensional MR Imaging: A Feasibility Study. Radiology 287(3):864-873.

56. Ferrero A, Ghelichkhan E, Manoochehri H et al (2024) A Pathologist-Guided and Explainable Workflow Using Histogram Embedding for Gland Classification. Mod Pathol 37(4):100447.

57. Goldenholz DM, Sun H, Ganglberger W, Westover MB (2023) Sam1ple Size Analysis for Machine Learning Clinical Validation Studies. Biomedicines 23:11(3):685.

58. Takayama Y, Nishie A, Sugimoto M et al (2016) Amide proton transfer (APT) magnetic resonance imaging of prostate cancer: comparison with Gleason scores. Magn Reson Mater Phy 29(4):671-679.

59. Evans VS, Torrealdea F, Rega M et al (2019) Optimization and repeatability of multipool chemical exchange saturation transfer MRI of the prostate at 3.0 T. J Magn Reson Imaging

50(4):1238-1250.

Figure legends

Fig. 1 Procedure for measuring the cell density in a cancerous region. The contour on the ADC map represents the cancerous region delineated by radiologists. A slice of the radical prostatectomy specimen, outlined in black, depicts the corresponding lesion area as delineated by pathologists. The cell density of the lesion was measured on the pathological image obtained from the specimen.

Fig. 2 Violin plots illustrating the distribution of cell density, with the median (open circle) and interquartile range (thick line) shown for each risk group (a) Low (GG ≤2, GS 3+3 and 3+4) and high (GG ≥3, GS 4+3 and above) GGs. (b) Low-, intermediate-, and high-risk groups. (c) TZ and PZ lesions. (d) GG 1, GG 2, GG 3, and GG 4 + GG 5.

Fig. 3 Heatmap of Spearman's rank correlation coefficient ρ between the cell density and all features in each risk group (significance threshold: *: $p<0.05$). GG, grade group; ADC, apparent diffusion coefficient; A-B, subtraction between A and B; H, high-pass filter Hist, histogram; JH, joint histogram; JH_A versus B, joint histogram between A and B; L, low-pass filter; WV, wavelet;

GLSZM, gray level size zone matrix; LGZE, low gray level zone emphasis; ZP, zone percentage; GLRLM, gray level run-Length matrix; LGRE, low gray level run emphasis; STD, standard deviation.

Fig. 4 Three PCa regions on the histopathological images (upper row), their corresponding 1st DCE images (middle row), and 5th DCE images (bottom row). White contours represent PCa regions in the DCE images.

655 **Supplementary Information**

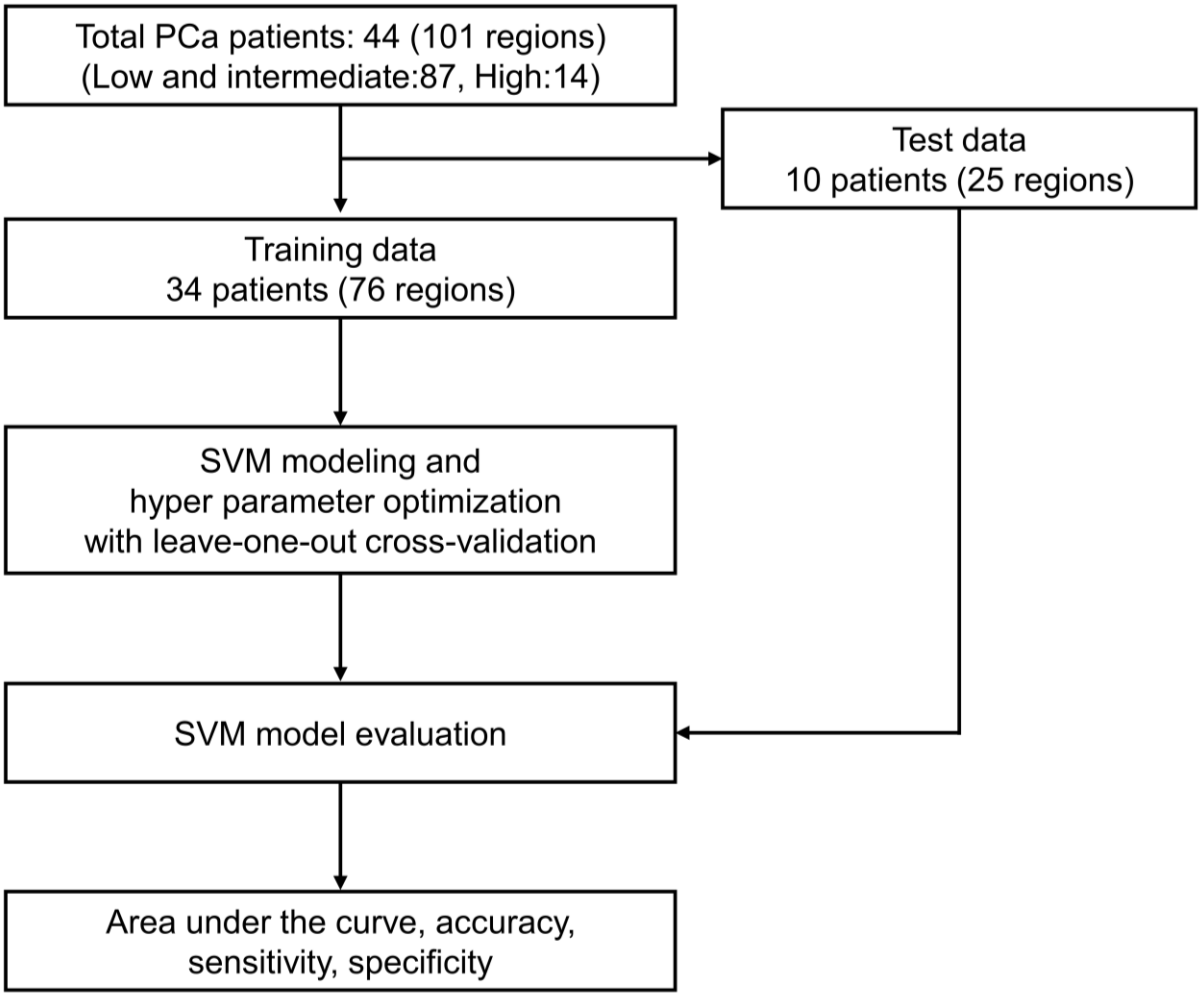

656

657 **Fig. S1** Workflow for training, testing, and evaluating the risk stratification model (SVM) for PCa